Estimation of a reliability range for the area-to-mass ratio of orbiters at the geostationary ring

Elvis Lacruz[a,*], Daniel Casanova[b,d], Alberto Abad[c,d]

[a]Centro de Investigaciones de Astronomía, Avd. Alberto Carnevalli, Sector La Hechicera, Edif. CIDA, Mérida, 5101, Venezuela.
[b]Centro Universitario de la Defensa de Zaragoza, Ctra. Huesca s/n, Academia General Militar, Zaragoza, 50090, España.
[c]Dpto. Física Teórica. Universidad de Zaragoza, Calle Pedro Cerbuna 12, Zaragoza, 50009, España.
[d]APEDIF - IUMA. Universidad de Zaragoza, Calle Pedro Cerbuna 12, Zaragoza, 50009, España.

Abstract

This paper shows the precise relative motion of different orbiters located at the geostationary region thanks to high precision astrometric coordinates, which are calculated thanks to different accurate observations taken from the Venezuelan National Observatory. These orbiters are close to each-other and present different relative motions although the magnitude of the distribution forces that act over them is the same. Thus, these orbiters must posses other intrinsic physic parameters which provokes the different observed morphological dynamic. In particular, the area-to-mass ratio could be one of them, and consequently, the main goal of this paper is to determine a reliability range for the area-to-mass ratio, that justifies the relative motion of these objects. Since a complete relative motion of the orbit is not feasible, we use realistic models to simulate the real motion of these orbiters, and we associate them an invented value for the area-to-mass ratio. Then, we use an analytical reduced model to compute the evolution of the eccentricity, considering different values for the area-to-mass ratio. Consequently, we are able to recover a reliability range for this invented parameter. In this work, it is also possible to consider the real ephemerides of objects listed in the CelesTrack database, and estimate its corresponding value for the area-to-mass ratio. Thus, this paper provides an innovative way to obtain a physical property of a space object just by observational information.

Keywords: Geostationary orbits, Space debris, Area-To-mass ratio, Relative motion, Temporal evolution.

1. Introduction

Since October 1957, when the launch of Sputnik I took place, humans have been leaving behind all kind of debris in space. The United Nations Committee on the Peaceful Uses of Outer Space (UNCOPUOS) defines Space Debris (SD) or orbital debris as all man-made objects, including fragments and elements thereof, in Earth orbit or re-entering the atmosphere that are useless[1].

There are three main regions where satellites are placed, and consequently, space debris is more noticeable; Low Earth Orbit (LEO), where satellites are orbiting at an altitude about 200 and 800 km, Medium Earth Orbit (MEO), where satellites are orbiting at an altitude up to 35000 km, and finally, Geostationary Orbit (GEO), where satellites are orbiting at a precise altitude of 35786 km (Chovotov, Herman & Johnson, 1997).

This paper is focused on the geostationary region, which is considered as a three dimensional torus centered at the equatorial plane at a geostationary altitude (McKnight & Di Pentino, 2013; ESA, 2019). This region is also named geostationary ring, which is delimited by the geostationary altitude (35786 km) ± 200 km, and the latitude ± 15° around the equatorial plane (IADC, 2007), which is an attractive region for its high commercial value, for placing communication, observation and broadcasting satellites since they have a fixed position in the sky with respect to a ground observer (Johnson et al., 2008).

Actually, in this region, we found active and non-active satellites, as well as space debris, which beginning to congest. The last one represents a larger population than satellites and it comes from different sources; nonfunctional spacecraft, explosions, collisions, satellite-surface degradation, operational debris separation, etc. (Smirnov, 2002). However, the main source of space debris have been different breakups that took place in the last years (Rykhlova, 2001; Africano, 2000; Petit et al., 2018). These space debris have been injected in different regions such as geostationary and graveyard orbits. Furthermore, nonfunctional satellites were abandoned in libration orbits with no intention of post-mission disposal, which lead to a higher concentration of defunct geostationary satellites in graveyard orbits (Klinrad, 2006). Although this region is protected, the number of operational spacecraft and debris at the geostationary ring is increasing continuously. This has increased the use of the high inclinations and eccentricities for GEO satellites and allows to higher hazard of that occur collisions (Johnson, 2012).

The orbital debris environment at the geostationary region has been investigated in the last two decades. The analysis of these population was based on available (real) and synthetic

*Corresponding author.
Email addresses: elvisjlc@gmail.com (Elvis Lacruz), casanov@unizar.es (Daniel Casanova), abad@unizar.es (Alberto Abad)

[1]Space Debris Mitigation Guidelines of the Committee on Peaceful Uses of Outer Space. United Nations. Vienna. 2010.

data, and different tools and methodologies have been developed to understand the real situation of space debris (Smirnov, 2002; Hanada & Yasaka, 2002; Celletti et al., 2017). In particular, EVOLVE, ORDEM 3.0 and MASTER-2009 are different software to model the current situation of space debris such as the flux, distribution mass, and other features of the space debris (Johnson et al., 2001; Englert, et al., 2014; Krisko et al., 2015). More recently, different features have been investigated by using statistical tools (Lewis et at., 2001; Englert, et al., 2014; Thomansson, Deleflie & Petit, 2019).

A qualitative and quantitative analysis of the current situation of the space debris population can allow to gain a better understanding of how geostationary space debris objects are generated and later accumulated. This analysis also condition the optimal use of the geostationary zone in the present and the near future. To that end, different mitigation strategies, safety operational maneuvers, risk of collision estimation, constant tracking services, between others, are developed. These strategies have had great attention by the scientific community because of their real and immediate implications (Anselmo & Pardini, 2002; Klinrad, 2006).

We should also take into account the long time of existence in orbit of these space debris objects and the difficulty of their disposal (Adushkin, et at., 2016). More precisely, the space debris generated in this particular region will stay there several decades, since there are no natural mechanisms such as the atmospheric drag that allow to decay these objects as occur in Low Earth Orbits (Colombo & Gkolias, 2017).

For all these reasons different tracking missions have been carried out through optical and telemetry surveys (Alby et al., 2004; Schildknecht et al., 2004; Flohrer et al., 2005; Laas-Bourez et al., 2011; Nuñez et al., 2015; Pradhan, Hickson & Surdej, 2019). Thus, thanks to the constant tracking, a detailed classification of space debris has been carried out in the last decades, however there is a lack of information of the physical and geometric features of these space debris objects. One of these physical properties is the area-to-mass (A/m) ratio, which is defined as the projected Sun facing area over the mass of the object. The projected Sun facing area is a function of the orientation of the space object, and consequently the effective area-to-mass ratio is time varying (Früh & Schidknecht, 2012). Thus, this parameter it is difficult to be estimated due to its time varying nature. Then, since the estimation of the area-to-mass ratio is a quite complex task, the goal of this paper is to give a suitable range for the area-to-mass ratio of a space debris object.

Focusing on the GEO region, as we illustrate in Fig. 1, the Keplerian perturbation is the dominant one, secondly we have the J_2 effect, and after we have the third body effect due to the Sun and the Moon. It is important to remark that the Solar Radiation Pressure (SRP) becomes the second disturbing force if the A/m ratio is big enough (i.e 40 m^2kg^{-1}), while if the ratio is smaller (about 1 m^2kg^{-1}) it has the same influence in the space object as the third body perturbation already mentioned. Other forces could be considered, but due to their smaller order of magnitude in comparison with the latest ones they are neglected in this work.

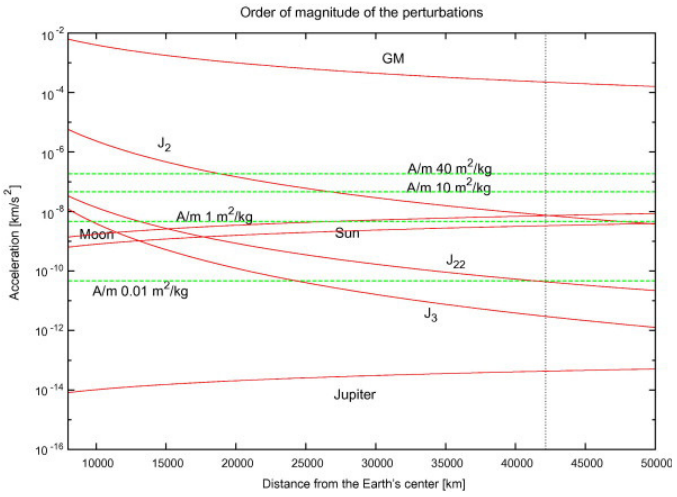

Figure 1: Order of magnitude of the perturbations (Valk, Lemaître & Anselmo, 2008).

It is known that, in this region, there are objects with an A/m ratio that varies up to 50 m^2kg^{-1} (Schildknecht, 2007; Pardini & Anselmo, 2008), which reveals a critical situation. A big value for the area-to-mass ratio is attributed to space debris, which are between 100 to 1000 times higher than the typical A/m ratio of a satellite in the GEO region (Schildknecht, Musci & Flohrer, 2008; Agapov, Molotov & Khutorovsky, 2009). As we already mentioned, the A/m ratio becomes an important parameter in the orbital evolution of space debris objects. In particular, the rise of this parameter leads to an increment in the amplitude of the oscillatory motion that is present in the temporal evolution of the eccentricity (Kuznetsov & Zakharova, 2015; Casanova, Petit & Lemaître, 2015). In addition, objects with high area-to-mass ratio present a very chaotic dynamic behavior compared to objects of low area-to-mass ratio in the same region (Valk et al., 2009). Consequently, the particular characteristics that are present in each piece of space debris (i.e the A/m ratio) provokes a different temporal evolution.

We have recall how important is the knowledge of the A/m ratio, and consequently, the more accurate this factor is, the better approximation of the space debris dynamics we have. Thus, an A/m ratio estimation will derive into a better knowledge of the space debris dynamics. The final goal of this work is to give a reliability range of the area-to-mass ratio of a given space object. Then, if we apply the estimated area-to-mass ratio to existing dynamical models we will determine in a better way the global dynamic of objects located at the geostationary region. This knowledge allows to establish control alerts for possible collision between objects orbiting in this region, allows space agencies to establish optimal conditions (and objectives) to protect the GEO ring for future space mission. Consequently, the estimation of the area-to-mass ratio of space debris objects is an urgent problem and becomes the final goal of this work.

The paper is organized as follows. Section 2, presents the current situation of orbiters in the GEO region, and shows the relative motion of some of them. It also illustrates how the relative motion of close orbiters is totally different under the same

perturbation effects, making their intrinsic physical characteristics the reason of having different dynamics. Section 3, introduces different ways of computing the temporal evolution of orbital elements of a space object. More precisely, we present the General Mission Analysis Tool (GMAT) software and an analytical methodology with a particular example. Section 4, shows different examples where the area-to-mass ratio is estimated, from real objects whose area-to-mass ratio was previously invented. Furthermore, we present how to use this tool to derive the area-to-mass ratio of objects whose ephemerides are in the CelesTrack database. Finally, in Section 5 we conclude the work.

2. Orbital motion in the geostationary ring

In this Section, we present the current situation of orbiters in the GEO region according to the existing literature. We also present the precise relative motion of some orbiters computed thanks to high precision astrometric observations from a CIDA survey on the GEO ring taken from the Venezuelan National Observatory (Lacruz & Abad, 2015; Lacruz et al., 2018a; , b). The purpose is to illustrate, that under the same perturbing effects, the relative motion of close space objects is completely different. The reason of this behaviour could be the intrinsic physical properties (such as the area-to-mass ratio) of the orbiters.

2.1. State of the Art

Objects located at the geostationary region present a particular property, they are in a 1:1 gravitational resonance with the Earth, where the orbital period corresponds to one sidereal day ($23^{\mathrm{h}}56^{\mathrm{min}}4^{\mathrm{s}}$). Then, an orbiter located at this region will present a fix position in an Earth Centered Earth Fixed (ECEF) reference frame, making this region very attractive for communication and observation satellites, because they have a fixed position in the sky with respect to a ground observer. Since there are hundreds of satellites in this region; it is expected several pieces of space debris. The debris population located at the GEO region come from different breakup events; according to (Rykhlova, 2001; Africano, 2000; ESA, 2019), there were several important breakup events. More precisely, there were five remarkable events (Petit et al., 2018) until 2016: Ekran-2 (1978/06/25), Titan Trans. 3C-5 (1992/02/21), Titan Trans. 3C-17 (2014/06/04), PROTON-M/BRIZ-M (2016/01/16), BEIDOU G2 (2016/06/29). Since then, there were many more: a minor breakup is associated with Titan 3C Transtage #1969-013B (2018/02/28), Atlas V Upper Stage Fragmentation Event (2018/08/31). In addition, there were many anomalous events that could be related to space debris collisions such as: AMC-9 (2017/06/17), TELKOM-1 (2017/08/30) and recently of the Intelsat 29E (2019/04/10) and future events, that for sure, will take place.

The above presented breakup events created thousands of space debris objects, which are distributed along this region. It is important to remark that in the GEO region, there are four equilibrium points, which are two stable and two unstable points, product of the non-uniform distribution of the Earth mass, more precisely due to the spherical harmonic J_2, C_{22}, and S_{22} that create these four equilibrium points (Morando, 1963; Soop, 1994). These points are localized at longitudes $\lambda_{s1} = 75°.1$ East, $\lambda_{s2} = 105°.3$ West, $\lambda_{u1} = 164$ East and $\lambda_{u2} = 11$ West (Capderou, 2005). Thus, orbiters located in this region transit irregularly between these equilibrium points (Wytrzyszczak, Breiter & Borczyk, 2007).

2.2. The relative motion of orbiters in the GEO ring

The natural motion of most orbiters in the GEO ring is without station-keeping thrust. Thus, they maintain a constant or nearly constant geometry of its relative orbit. In particular, the projection of the relative motion over the Earth surface it is not exactly a fixed point respect to the Earth Centered Earth Fixed (ECEF) reference frame. Its path becomes less symmetric and distorted and it recalls to a Bernoulli lemniscate.

In order to know precise relative motion of some orbiters, we consider the high precision astrometric positions from a CIDA survey on the GEO ring taken from the Venezuelan National Observatory. The angular positions of those objects are calculated with a high astrometric precision, where the errors are of the order to $0''.12$ and $0''.11$ in the topocentric equatorial coordinates, respectively (Lacruz et al., 2018).

In Figs. 2 and 3 we show the angular positions of five orbiters which are located at different longitudes. We select the sub-satellite points $\lambda_{GEO} = 24°.80$, $34°.55$, $61°.55$ and $71°.05$ W, that are available into the CIDA survey data set. More precisely, in these plots we show a section of the orbital relative motion in function of time, corresponding to 110 min of the orbital period for each orbiter. The process pipeline was made taking thirty-six astrometric observations (for each λ_{GEO}). Remark that each set of thirty-six astrometric observations is divided in six subsets of observations. The interval of time between the first and the last one is 110 min, taking into account the following: (1) 10 s of integration time of each observation; (2) the delay time for downloading the CCD image; and (3) 540 s of separation between each subset. The set of points in each panel represents the real position at each instant of time of observation. In Table 1 we provide the variation of the angular position of the objects located in the λ_{GEO} in term of pixels and arc-seconds, taking into account that 1 pixel is equal to $0''.546$.

Remark that in the lower panel of the Fig. 3 we have two orbiters, whose motion direction are opposite. The upper orbiter presents a smaller variation than the lower one in the $x-$axis, while the upper orbiter presents a greater variation than the lower one in the $y-$axis. Thus, in the same sub-satellite point $\lambda_{GEO} = 70°.05$ W we have two different orbiters with a completely different relative orbital motion.

Therefore, the relative motion that we observe in each nominal window is not equal for all orbiters. We observe different morphological dynamics for each orbiter. Taking into account that the magnitude of the distribution forces that act over these orbiters is the same (Valk, Lemaître & Anselmo, 2008), and they are close each other, there must be other intrinsic physic parameters in the orbiters which provokes the different observed morphological dynamics. A possible explanation of this behaviour could be an intrinsic physical parameter such as

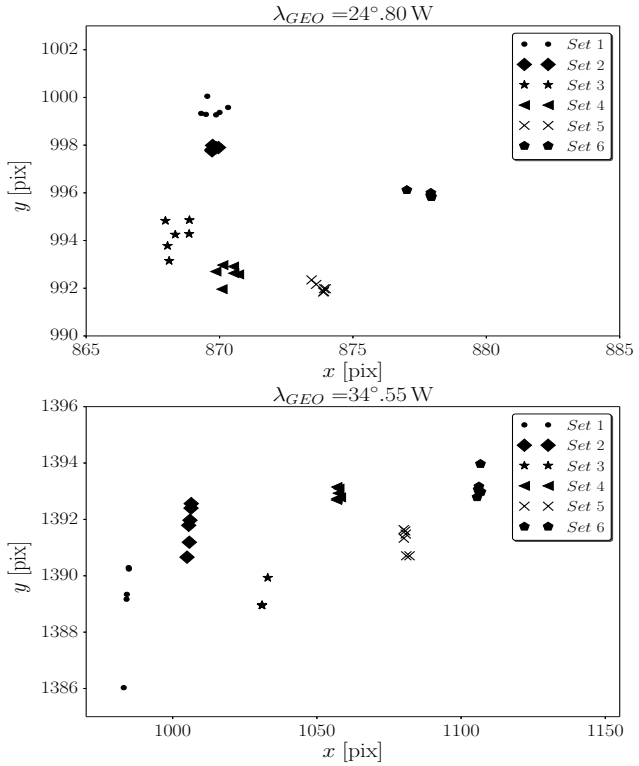

Figure 2: Orbiters located at λ_{GEO} = 24°.80 W (upper panel) and λ_{GEO} = 34°.55 W (lower panel). In both panels it is showed the relative motion of the orbiters during 110 minutes. It is also possible to know the shape of the relative orbit by joining the data set from 1 to 6. The error bars, which indicate the precision of the relative orbit, are smaller than symbols and they are not appreciated.

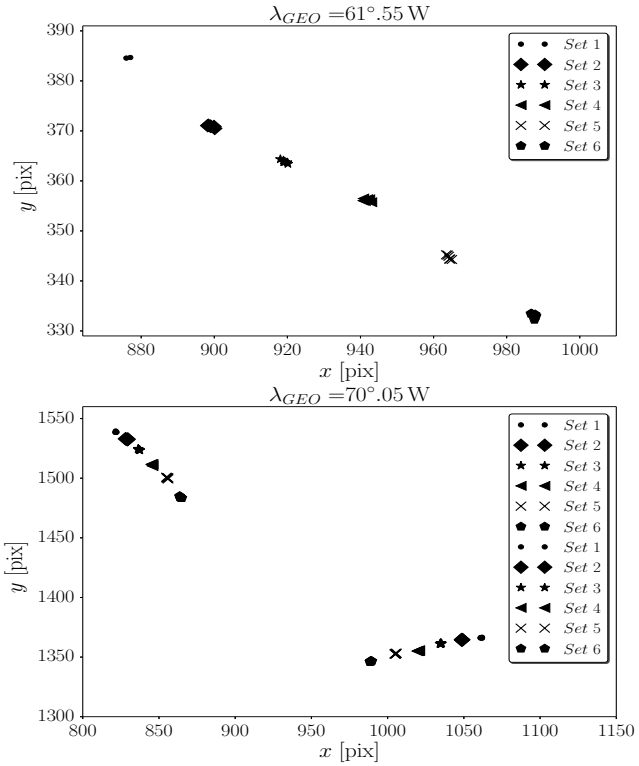

Figure 3: Orbiters located in λ_{GEO} = 61°.55 W (upper panel) and λ_{GEO} = 70°.05 W (lower panel). In both panels it is showed the relative motion of the orbiters during 110 minutes. It is also possible to know the shape of the relative orbit by joining the data set from 1 to 6. At λ_{GEO} = 70°.05 W there are two different orbiters. The error bars, which indicate the precision of the relative orbit, are smaller than symbols and they are not appreciated.

Table 1: Variation of the relative motion during 110 minutes of the orbiters located in different λ_{GEO} at the geostationary ring. The displacements Δ_x and Δ_y, in pixels, equivalently Δ_α and Δ_δ, in arcsec. Take into account that 1 pix = $0''.546$.

Orbiter # Figs.	λ_{GEO} (°) W	Δ_x (pix)	Δ_y (pix)	Δ_α ($''$)	Δ_δ ($''$)
2. (upper panel)	24.80	10.70	9.60	5.84	5.24
2. (lower panel)	34.55	25.30	9.80	13.81	5.35
3. (upper panel)	61.55	51.85	111.83	28.31	61.05
3. (lower panel) (upper left)	70.05	20.57	73.46	11.23	40.11
3. (lower panel) (lower right)	70.05	43.68	55.04	23.83	30.05

the A/m ratio, which is a priory unknown, and difficult to determine accurately.

In the following Section we present different tools, which are useful to know the dynamics of orbiters in the GEO ring.

3. Temporal evolution of the orbital elements

In this section, we present different tools for computing the temporal evolution of a space object. We introduce the General Mission Analysis Tool (GMAT), which is an open source software system for space mission design, optimization, and navigation (`https://software.nasa.gov/`). After that, we present an analytical methodology for computing the temporal evolution of a space object located at the GEO region. Finally, we provide an example to illustrate the different tools.

3.1. General Mission Analysis Tool (GMAT)

The GMAT supports missions in flight regimes ranging from low Earth orbit to lunar, libration points, and deep space missions. However, we focus our analysis on the GEO ring. Since GMAT contains models of real world objects such as spacecraft and thrusters, and it is possible to include several distributing forces when propagating a space object, we consider this numerical tool as a realistic way to compute the evolution of different orbiters.

3.2. Analytical methodology

In this subsection we recall an analytical tool for computing the temporal evolution of space debris located at the GEO region, that is orbiting around the Earth (see (Casanova, Petit & Lemaître, 2015) for a more detailed explanation). This analytical model considers the non-uniform distribution of the Earth mass (more specifically, the Earth oblateness or the J_2 effect), the gravitational potential due to the Sun and the Moon effect (Montenbruck, 2005; Pardini & Anselmo, 2008) as third bodies, and the Solar Radiation Pressure (SRP), neglecting the remaining perturbing forces.

The classical orbital elements are the semi-major axis (a), eccentricity (e), inclination (i), right ascension of the ascending node (Ω), argument of perigee (ω) and mean anomaly (M). However, this analytical tool avoids these classical orbital elements and uses the Poincaré's Variables, which are canonical and non-singular. These variables, which avoid problems when the inclination or the eccentricity become zero, are the following:

$$\begin{aligned} x_1 &= \sqrt{2\,P}\sin p, & y_1 &= \sqrt{2\,P}\cos p,\\ x_2 &= \sqrt{2\,Q}\sin q, & y_2 &= \sqrt{2\,Q}\cos q,\\ \lambda, & & L, & \end{aligned}$$

where λ is the mean longitude, which represents the mean anomaly (M) plus the argument of perigee (ω) plus the longitude of the ascending node (Ω). L is one of the Delaunay's elements and is given by:

$$L = \sqrt{\mu\,a}, \quad G = \sqrt{\mu\,a(1-e^2)}, \quad H = \sqrt{\mu\,a(1-e^2)}\cos i,$$

being $\mu = \mathcal{G}\,M_\oplus$ with $\mathcal{G}$ the standard gravitational constant, $M_\oplus$ the mass of the Earth. Finally, P, Q, p and q are the modified Delaunay's elements, given by:

$$\begin{aligned} P &= L - G, & p &= -\omega - \Omega,\\ Q &= G - H, & q &= -\Omega. \end{aligned}$$

Given the generalized coordinates (p, q, λ) (or the position $\mathbf{r}$) and the generalized momenta (P, Q, L) (or velocity $\mathbf{v}$) of a space object, it is possible to describe its motion thanks to the following Hamiltonian formulation:

$$\begin{aligned} \dot{p} &= \frac{\partial \mathcal{H}}{\partial P}, & \dot{P} &= -\frac{\partial \mathcal{H}}{\partial p},\\ \dot{q} &= \frac{\partial \mathcal{H}}{\partial Q}, & \dot{Q} &= -\frac{\partial \mathcal{H}}{\partial q},\\ \dot{\lambda} &= \frac{\partial \mathcal{H}}{\partial L}, & \dot{L} &= -\frac{\partial \mathcal{H}}{\partial \lambda}, \end{aligned}$$

where the Hamiltonian function is given by:

$$\begin{aligned} \mathcal{H}(\mathbf{r}, \mathbf{v}, \mathbf{r}_\odot, \mathbf{r}_{\leftmoon}) &= H_{kepler}(\mathbf{r}, \mathbf{v}) + H_{J_2}(\mathbf{r}) +\\ &+ H_{SRP}(\mathbf{r}, \mathbf{r}_\odot) +\\ &+ H_{3bS}(\mathbf{r}, \mathbf{r}_\odot) + H_{3bM}(\mathbf{r}, \mathbf{r}_{\leftmoon}), \end{aligned} \tag{1}$$

where $\mathbf{r}$ and $\mathbf{v}$ are the Cartesian geocentric coordinates and velocities of any space object in the GEO region, $\mathbf{r}_\odot$ the Cartesian geocentric coordinates of the Sun and $\mathbf{r}_{\leftmoon}$, these of the Moon. All of them are given with respect to an inertial equatorial geocentric reference frame. Hereinafter, we denote by $r = \|\mathbf{r}\|$, $r_\odot = \|\mathbf{r}_\odot\|$, $r_{\leftmoon} = \|\mathbf{r}_{\leftmoon}\|$, and $v = \|\mathbf{v}\|$.

The Hamiltoninan given in Eq. (1) is split in different parts, where H_{kepler} represents the attraction of the Earth as a central body, H_{J_2} the potential function that affects the space object due to the Earth oblateness. We only consider the zonal harmonic J_2, which is the most representative of the potential function. H_{SRP} represents the direct solar radiation pressure potential and it is strongly related with A/m ratio, H_{3bS} the effect of the Sun, as third body, and H_{3bM} this of the Moon.

Several periods are present in the Hamiltonian, a 1-day-period (for geostationary orbit), a 1-month-period (in the Moon motion), a 1-year-period (in the Sun motion), periods linked to the J_2 perturbation, and longer periods that appear clearly

in the numerical integration. Thus, thanks to several averaging process we are able to obtain analytical expressions for the variables x_1, x_2, y_1 and y_2 and consequently, we are able to recover from them the temporal evolution of the e, i, Ω and ω of a space object. We summarize the analytical expressions of the variables. For short periods of time, of a few years, the result (Casanova, Petit & Lemaître, 2015) is simply:

$$\begin{aligned} x_1(t) &= C_x + \frac{k\,\sin(n_\odot\,t+\lambda_{\odot,0})}{1-\eta^2}\,[\eta\,\cos\epsilon+1]\,, \\ y_1(t) &= C_y + \frac{k\,\cos(n_\odot\,t+\lambda_{\odot,0})}{1-\eta^2}\,[\cos\epsilon+\eta]\,, \end{aligned} \tag{2}$$

where the values for C_x and C_y are fixed by the initial conditions ($t = 0$). Furthermore, it has been assumed a circular motion for the Sun, only depending on its mean longitude $\lambda_\odot = n_\odot\,t + \lambda_{\odot,0}$ (with $n_\odot = 2\,\pi\,\mathrm{yr}^{-1}$ and $\lambda_{\odot,0}$ the initial position of the Sun) and on the Earth's obliquity ϵ. Finally, the values for η and k are given by:

$$\eta = \frac{C_2}{n_\odot}, \qquad n_\odot\,k = \frac{3}{2}\,C_r\,P_r\,\frac{A}{m}\,\frac{a}{\sqrt{L}},$$

where $C_2 = \frac{3}{2}\sqrt{\frac{\mu}{a^3}}\,\mathrm{J}_2\,\frac{r_\oplus^2}{a^2}$ being, $r_\oplus$ the Earth radius, and a the semi-major axis of the space debris object. Finally, the parameter C_r (fixed to 1 in this paper) is a dimension-free reflectivity coefficient, $Pr = 4.56\times10^{-6}\,\mathrm{Nm}^{-2}$ is the radiation pressure for an object located at a distance of 1 au from the Sun, A/m is the area-to-mass ratio of the space debris given in $\mathrm{m}^2\mathrm{kg}^{-1}$ and $a_\odot$ is equal to the mean distance between the Sun and the Earth (i.e. $a_\odot = 1$ au). We consider that $r_\odot \simeq a_\odot$.

Thanks to a second averaging process (over 1 year) and taking into account the obtained expressions for x_1 and y_1 it is possible to obtain analytical expressions for x_2 and y_2, that are given by:

$$\begin{aligned} x_2(t) &= \mathcal{D}\,\sin(\sqrt{g_1\,g_2}\,t-\psi), \\ y_2(t) &= \mathcal{D}\,\sqrt{\frac{g_2}{g_1}}\,\cos(\sqrt{g_1\,g_2}\,t-\psi)-\frac{g_3}{g_1}. \end{aligned} \tag{3}$$

These equations represent an oscillatory motion, $\mathcal{D}$ is the amplitude and ψ the phase space. Both of them are calculated through the initial conditions. The variables g_1, g_2 and g_3 are given by:

$$\begin{aligned} g_1 &= n_\odot\,\frac{k^2}{4\,L}\,\cos\epsilon+\frac{C_q}{2}-\delta-\delta\,\cos 2\epsilon-\gamma-\gamma\,\cos\epsilon_M, \\ g_2 &= n_\odot\,\frac{k^2}{4\,L}\,\cos\epsilon+\frac{C_q}{2}-2\,\delta\,\cos 2\epsilon-2\,\gamma\,\cos 2\epsilon_M, \\ g_3 &= -n_\odot\,\frac{k^2}{2\,\sqrt{L}}\,\sin\epsilon+2\,\delta\,\sqrt{L}\,\sin 2\epsilon+2\,\gamma\,\sqrt{L}\,\sin 2\epsilon_M, \end{aligned}$$

where ϵ_M is the obliquity of the Moon, the variable C_q is computed by considering the value $i = 0°$, in agreement with the truncation in i^2, and we replace e by its averaged value, $\bar{e}$, over $\lambda_\odot$, that is,

$$C_q = C_2\,(1+2\,\bar{e}^2), \tag{4}$$

and finally, the parameters δ and γ, which are given by:

$$\delta = \beta\,\frac{3\,a^2}{16\,L\,a_\odot^2}, \qquad \gamma = -\frac{\mu_\leftmoon}{a_\leftmoon}\,\frac{3\,a^2}{16\,L\,a_\leftmoon^2},$$

Table 2: Initial condition of the orbiter with semi-major axis, a, eccentricity, e, inclination, i, right ascension of the ascending node, Ω, argument of perigee, ω, mean anomaly, M, and the area-to-mass, A/m, ratio.

Initial date	January 01, 2018. $0^\mathrm{h} : 0^\mathrm{min} : 0^\mathrm{s}.0$
Final date	January 01, 2019. $0^\mathrm{h} : 0^\mathrm{min} : 0^\mathrm{s}.0$
a	42164.0 km
e	0.000272900
i	0°.784092740
Ω	90°.245499999
ω	335°.171400659
M	201°.927300003
A/m	0.25000 (2.5/10) $\mathrm{m}^2\mathrm{kg}^{-1}$

where β is given by:

$$\beta = \left[C_r\,P_r\,\frac{A}{m}\,a_\odot - \frac{\mu_\odot}{a_\odot}\right], \tag{5}$$

$\mu_\odot = \mathcal{G}\,M_\odot$ with $M_\odot$ the mass of the Sun, and $\mu_\leftmoon = \mathcal{G}\,M_\leftmoon$ with $M_\leftmoon$ the mass of the Moon, and ϕ_M representing the angle between the satellite and the Moon positions. The motion of the Moon is also assumed to follow a circular orbit, i.e. $r_\leftmoon = a_\leftmoon$.

Remark that Eqs. (2) and Eqs. (3) are the analytical solution of the problem of a space object orbiting around the Earth in the GEO ring.

Note that during the previous procedure we average the Hamiltonian function over the mean longitude (λ) since, for long-time propagation, the short periodic oscillations caused by the mean longitude are meaningless. Thus, under the averaging assumption, our problem becomes a four degree of freedom problem in the averaged variables x_1, y_1, x_2 and y_2, since the mean longitude is not present anymore; consequently the semi-major axis (a) or the momentum associated to the mean longitude (L) will be constants.

3.3. Evolution of a space debris object

At this point, given the information of a particular object located at the GEO ring, it is possible to compute its ephemerides. To that end, we use different tools such as the CelesTrack database, and the two presented tools: GMAT and the analytical method. More precisely, we calculate the temporal evolution of the osculating orbital elements. However, as we already mention, since the analytical methodology averages over the mean anomaly (and consequently the semi-major axis remains constant) we focus our study into the remaining four variables and more specifically into the eccentricity and inclination.

We consider an orbiter whose initial conditions are in Table 2. First of all, by using the GMAT tool, we compare the temporal evolution of the orbiter computed by a realistic model versus a reduced model. The realistic model considers: gravitational model JGM-2 (Tapley et al., 1996) of degree 70 and order 70, the third body perturbation due to the Sun, Moon, Jupiter and Saturn, the solar radiation pressure with a spherical model and without the shadowing effects, between others. The reduced model considers: gravitational model JGM-2 of degree

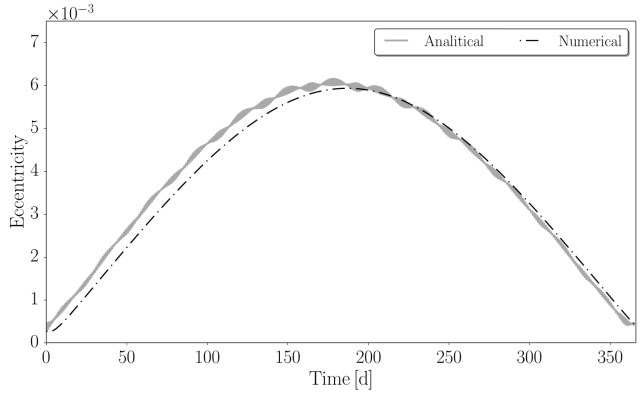

Figure 4: Evolution of the eccentricity during 1 year, of the virtual space object in the reduced numerical model (dash-dotted line) versus the analytical one (solid line). The initial conditions are the ones presented in Table 2.

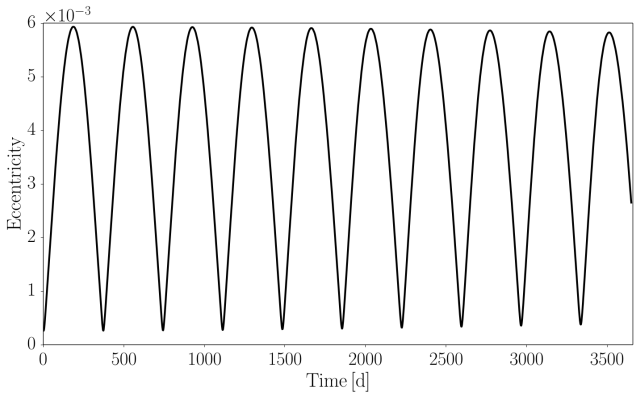

Figure 5: Evolution of the eccentricity during 10 years of the virtual space object. The initial conditions are the ones presented in Table 2.

2 and order 0, the third body perturbation due to the Sun and Moon, and the solar radiation pressure effect.

As a conclusion of this comparison, we obtain that the reduced model is a reliable one, since the difference between the realistic and the reduced model is not relevant. As a quantitative analysis, the relative errors in the eccentricity is of order 10^{-10} , and in the inclination is of order 10^{-9}. This is an expected result since, as we already show in Fig. 1, the most important perturbations that need to be considered in the GEO region are the ones that are included in the reduced model.

Now, we compare the reduced model of GMAT with the analytical model in order to confirm the reliability of the last. In Fig. 4 we compare the temporal evolution of the eccentricity during one year of a virtual orbiter, whose initial conditions are given in Table 2. The numerical approach with the reduced model of GMAT give similar plots as the obtained with the analytical tool, and consequently, we can use the analytical method since it is simpler, quick and provides a reliable approach of the temporal evolution (See (Casanova, Petit & Lemaître, 2015) for a detailed comparison).

In the case of the inclination, one year is not enough to show its variation. In Figs. 5 and 6, we plot the temporal evolution of the eccentricity and inclination of the orbiter during ten years. Note that it is observable the periodic motion of one year in the eccentricity, while it is not in the inclination. For this reason, we plot in Fig. 7 the evolution of the inclination during 200 yrs, where the long periodic motion of about 56 yrs it is observable. This justifies why we consider only the evolution of the eccentricity in this study, since the variation of the inclination is observable for long periods of time.

Remark that, the bigger the A/m of the space object is, the bigger the amplitude of the eccentricity is. Furthermore, the amplitude of the inclination (in this case less than 1°) is at most 14°, which is in agreement with the amplitude of the periodic motion of the inclination of the objects located at the GEO region.

We have shown the temporal evolution of the eccentricity and inclination of an orbiter. Note that in this particular case the A/m is an input parameter. The idea of this work is to estimate this

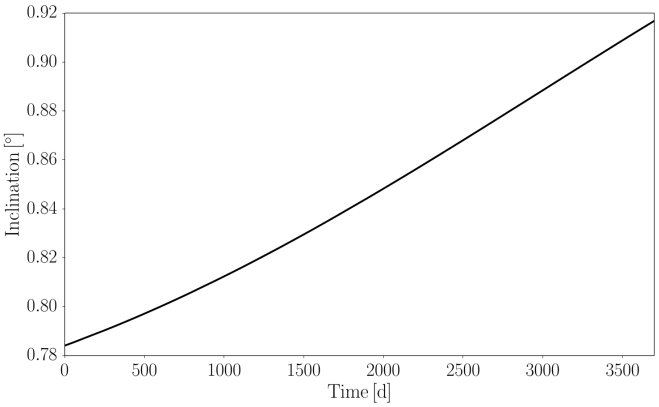

Figure 6: Evolution of the inclination during 10 years of the virtual space object. The initial conditions are the ones presented in Table 2.

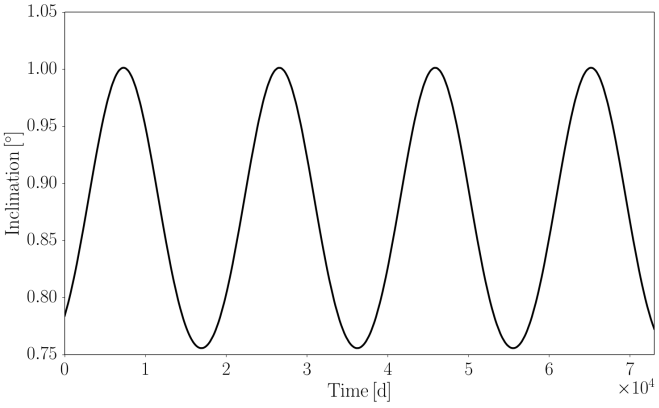

Figure 7: Evolution of the inclination during 200 years of the virtual space object. The initial conditions are the ones presented in Table 2.

parameter from real data or in our case a realistic model from GMAT. Then, in the following section we give a reliability band of the area-to-mass ratio of a given orbiter in the GEO ring, estimating a physical property (the area-to-mass ratio) from its dynamics.

4. Estimation of the area-to-mass ratio

In this section we explain how to determine a reliability band of the area-to-mass (A/m) ratio of an orbiter located at the GEO ring, which are contained in the NASA NORAD Catalog. First, we give an invented value for this parameter and we compute its orbital motion by using the realistic model of GMAT. Then, it is possible to recover the invented value of the area-to-mass ratio or at least to determine a reliability band of this parameter by using the analytical method. Second, we use the CelesTrack information, where it is possible to obtain the ephemerides of space objects. By using that information, we are able to determine a reliability band of the area-to-mass (A/m) ratio of the space object obtaining a physical property (the area-to-mass ratio) from the CelesTrack data.

4.1. Recovering an invented value for the area-to-mass ratio of an orbiter

We consider realistic objects, which are listed in the NASA NORAD Catalog. Each object has a NORAD ID, which is a sequential 5-digit number assigned by the United States SPACE COMmand (USSPACECOM) to all Earth orbiting satellites in order of identification.

From the Two Line Elements data set we obtain the following: Julian Date (JD), semi-major axis (a), eccentricity (e), inclination (i), right ascension of the ascending node (Ω), argument of perigee (ω) and mean anomaly (M). We also have information about the BSTAR ($B^\star$) coefficient, which is strongly related with the A/m ratio ($B^\star \propto A/m$). However, all cases of study have this parameter equal to zero. It does not mean necessarily that the value is zero, it could mean that the value is unknown.

At this point we consider as a first example the object with NORAD ID 33595, whose initial conditions are illustrated in Table 3. We consider an invented value $A/m = 0.0075\,\mathrm{m^2kg^{-1}}$ for this particular orbiter. Then, we compute the temporal evolution of the eccentricity by using the realistic GMAT model, and we use the analytical method also to compute the temporal evolution of the eccentricity, but this time considering different area-to-mass ratios. The idea is to fit the realistic evolution with one or several of the analytical evolution, which are different since we provide different values for the area-to-mass ratio.

In Fig. 8 shows the temporal evolution of the eccentricity of the object with NORAD ID 33595. We plot the evolution computed with the realistic GMAT model with an invented value for the $A/m = 0.0075\,\mathrm{m^2kg^{-1}}$. We also plot the temporal evolution of the eccentricity computed with the analytical method by using different A/m ratios. The upper curve is associated with the A/m equal to $0.05\,\mathrm{m^2kg^{-1}}$ and the lower curve is associated with the A/m equal to $0.001\,\mathrm{m^2kg^{-1}}$. It is possible to refine the upper

Table 3: Initial condition of the orbiter with NORAD ID 33595. Julian Date (JD), semi-major axis, a, eccentricity, e inclination, i, right ascension of the ascending node, Ω, argument of perigee, ω and mean anomaly, M.

JD	2457025.367446810007
a	42164.81494093991 km
e	3.26×10^{-5}
i	$1^\circ.83000003 \times 10^{-3}$
Ω	235°.3125
ω	117°.525999998775
M	139°.8608000002993

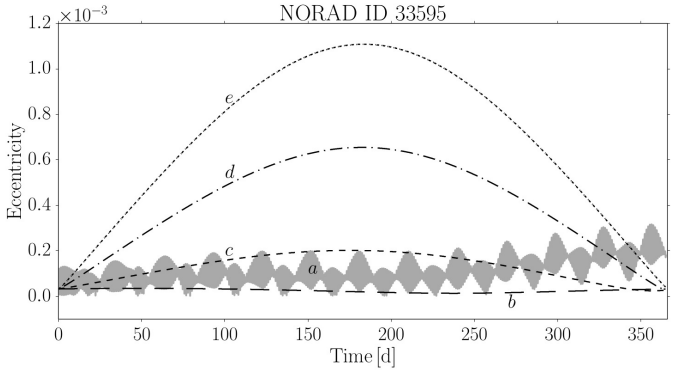

Figure 8: Evolution of the eccentricity during 1 year of the orbiter with NORAD ID 33595. Realistic GMAT model with an invented value of $A/m = 0.0075\,\mathrm{m^2kg^{-1}}$, represented by the solid line (a). The analytical approach is computed taking into account different values for the A/m ratio. More precisely, 0.001, 0.01, 0.03 and 0.05 $\mathrm{m^2kg^{-1}}$, which are represented by the dashed lines (b), (c), (d) and (e), respectively. A suitable reliability band for the area-to-mass ratio of this object is 0.001-0.01 $\mathrm{m^2kg^{-1}}$.

value and, as we can see in the plot, we determine a reliability band for the A/m parameter of 0.01-0.001 $\mathrm{m^2kg^{-1}}$. This means that we recover successfully the invented value for the area-to-mass ratio of the space object since $0.0100 \leq 0.0075 \leq 0.0010$. This is a suitable band for the parameter taking into account that, a priori, is unknown.

We did similar research with other space debris objects, whose initial values for the eccentricity and inclination are given in Table 4 considering the information of CelesTrack database.

Figs. 9, 10 and 11 show the temporal evolution of the eccentricity of the space objects with NORAD ID 25354, 32768 and

Table 4: Initial conditions of space debris objects in the geostationary ring from CelesTrack database. The columns represent the NORAD ID, Julian Date (JD), eccentricity (e), inclination (i) and the invented value for the area-to-mass ratio (A/m). The last one (ID 12345) is an invented object with a high value for the are-to-mass ratio.

NORAD ID	JD	e	i (°)	A/m $\mathrm{m^2kg^{-1}}$
33595	2457025.3674468	0.0000326	0.0183	0.0075
25354	2457024.9065858	0.0002901	0.0240	0.0833
32768	2457024.5637829	0.0002315	0.0291	0.2500
41836	2457702.9975671	0.0000404	0.0711	0.0010
12345	2458484.5000000	0.0002729	0.0041	25.000

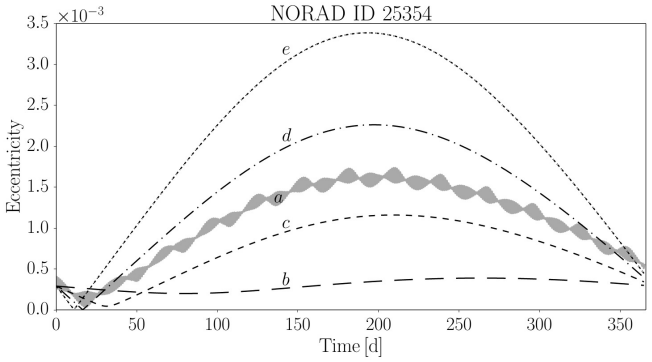

Figure 9: Evolution of the eccentricity during 1 year of the orbiter with NORAD ID 25354. Realistic GMAT model with an invented value of A/m = 0.0833 m^2kg^{-1} represented by the solid line (*a*). The analytical approach is computed taking into account different values for the A/m ratio. More precisely, 0.009, 0.050, 0.100 and 0.150 m^2kg^{-1}, which are represented by the dashed lines (*b*), (*c*), (*d*) and (*e*), respectively. A suitable reliability band for the area-to-mass ratio of this object is 0.05- 0.10 m^2kg^{-1} since 0.0500 ≤ 0.0833 ≤ 0.100.

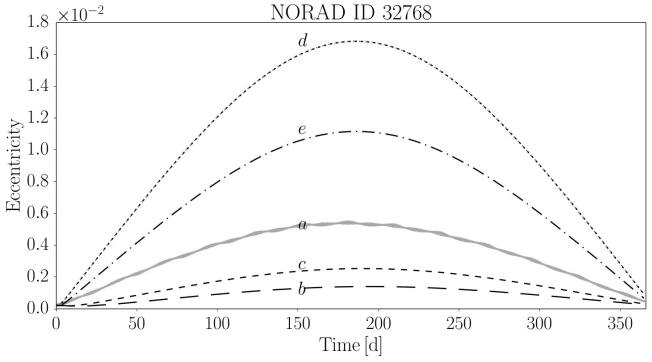

Figure 10: Evolution of the eccentricity during 1 year of the orbiter with NORAD ID 32768. Realistic GMAT model with an invented value of A/m = 0.25 m^2kg^{-1}, represented by the solid line (*a*). The analytical approach is computed taking into account different values for the A/m ratio. More precisely, 0.07, 0.12, 0.50 and 0.75 m^2kg^{-1}, which are represented by the dashed lines (*b*), (*c*), (*d*) and (*e*), respectively. A suitable reliability band for the area-to-mass ratio of this object is 0.12-0.50 m^2kg^{-1} since 0.1200 ≤ 0.250 ≤ 0.500. In this particular case, we observe that the value A/m = 0.250 m^2kg^{-1} in the analytical method almost reproduce the realistic approach.

41836, respectively. We consider different and invented values for the area-to-mass ratio equal to 0.083, 0.25 and 0.001 m^2kg^{-1}, respectively. These values are used in the realistic GMAT model. In these figures we also plot the temporal evolution of the eccentricity, computed with the analytical method but using different area-to-mass ratios. These temporal evolution are plotted with the solid lines. For each particular space object we are able to determine a reliability band for the area-to-mass ratio in accordance with the invented value. Thus, the reliability bands for the space objects with NORAD ID 25354, 32768 and 41836 the A/m ratio are 0.05-0.1, 0.12-0.5 and 0.001-0.005 m^2kg^{-1}, respectively and represented by the dashed lines in each figure.

Finally, in Fig. 12 we show the temporal evolution of an orbiter with a high area-to-mass ratio in order to test the methodology with this kind of orbiters. More precisely, we compute the temporal evolution of eccentricity in a realistic GMAT model with a given value for the area-to-mass ratio equal to 25.0 m^2kg^{-1}. We also plot the computed temporal evolution with the analytical model considering different values for the area-to-mass ratio. More precisely, we consider a range o values from 20 to 30 m^2kg^{-1} and we observe how the analytical evolution fits the realistic evolution. We conclude that this methodology it is also useful with objects with high area-to-mass ratio. In this particular example we observe that a reliability band for the area-to-mass ratio could be 24-26 m^2kg^{-1}, which is in accordance with the invented value for the A/m ratio.

Until now, we use real orbiters (with an artificial A/m ratio) and we succeed with the estimation of the area-to-mass ratio of the object. Now, it is time to proceed in an inverse way, i.e, we observe the evolution of the eccentricity of a real object and we obtain a range of values for the area-to-mass ratio that could be associated to the real object.

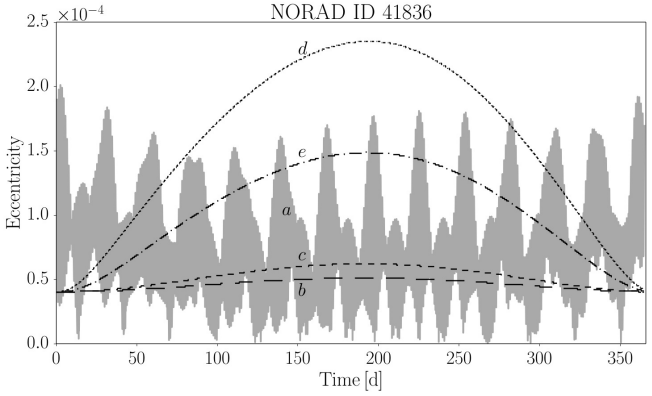

Figure 11: Evolution of the eccentricity during 1 year of the orbiter with NORAD ID 41836. Realistic GMAT model with an invented value of A/m = 0.001 m^2kg^{-1}, represented by the solid line (*a*). The analytical approach is computed taking into account different values for the A/m ratio. More precisely, 0.0005, 0.001, 0.005 and 0.009 m^2kg^{-1} which are represented by the dashed lines (*b*), (*c*), (*d*) and (*e*), respectively. A suitable reliability band for the area-to-mass ratio of this object is 0.001-0.005 m^2kg^{-1} since 0.001 ≤ 0.001 ≤ 0.005. In this particular case, the area-to-mass ratio is so small that is difficult to give a precise reliability band.

4.2. Estimation of the area-to-mass ratio by using the CelesTrack data

In this subsection we obtain a reliable band of values for the A/m ratio of a real object by using the information coming from the CelesTrack database. We select a real object with NORAD ID 33595, whose ephemerides are known.

In Fig. 13 we plot the temporal evolution of the eccentricity of the object with NORAD ID 33595 by using the ephemerides of the object coming from the CelesTrack database. As we observe previously, if we change in the analytical method the value of the A/m ratio, the temporal evolution of the eccentricity is also changing. Thus, we fit the eccentricity evolution from CelesTrack data with a suitable evolution for the eccentricity by trying different A/m ratios. More precisely, the upper line shows the evolution of the eccentricity if a value for the A/m equal to 0.01 m^2kg^{-1} is considered, and a the lower dashed line

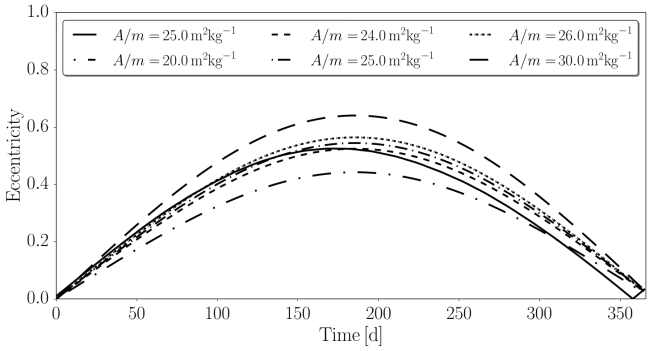

Figure 12: Evolution of the eccentricity during 1 year of an invented orbiter with a given area-to-mass ratio. Realistic GMAT model with an invented value of $A/m = 25\,\mathrm{m^2kg^{-1}}$, represented by the solid line. The analytical approach is computed taking into account different values for the A/m = ratio. More precisely, 20, 24, 25, 26, and 30 $\mathrm{m^2kg^{-1}}$, which are represented by the dashed lines, bottom up, respectively. A suitable reliability band for the area-to-mass ratio of this object is 24-26 $\mathrm{m^2kg^{-1}}$, which is in accordance with the given value for A/m.

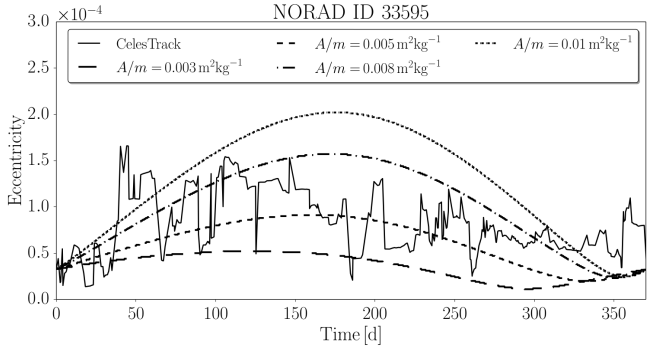

Figure 13: Temporal evolution of the eccentricity during 1 year of the orbiter with NORAD ID 33595. The CelesTrack data is represented with the solid line. The analytical approach is computed taking into account different values for the A/m ratio. More specifically, 0.003, 0.005, 0.008 and 0.01 $\mathrm{m^2kg^{-1}}$, which are represented by the dashed lines, bottom up, respectively.

shows the evolution of the eccentricity if a value for the A/m equal to 0.003 $\mathrm{m^2kg^{-1}}$ is considered. Consequently, it is possible to establish a reliability band for the A/m ratio of this object of 0.003-0.01 $\mathrm{m^2kg^{-1}}$.

In addition to that, we plot in Fig. 14 the behaviour of the eccentricity during three years. We observe that the eccentricity evolution plotted by using the CelesTrack information suites very well with the two analytical eccentricity evolution with associated values for the area-to-mass ratio equal to 0.003 and 0.01 $\mathrm{m^2kg^{-1}}$, respectively.

We did similar research with the orbiter with NORAD ID 40875. In Fig. 15 we show the temporal evolution of the eccentricity with the data coming form CelesTrack, represented by the solid line, and the computed evolution with the analytical method with different area-to-mass ratios, which are represented by the dashed lines, bottom up, respectively.

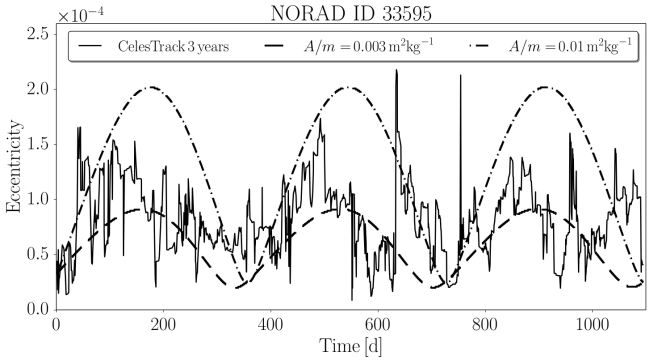

Figure 14: Temporal evolution of the eccentricity during 3 years of the orbiter with NORAD ID 33595, represented by the solid line. The CelesTrack data are represented with the solid line. The analytical approach is computed taking into account different values for the A/m ratio. More precisely, 0.003-0.01 $\mathrm{m^2kg^{-1}}$, which represent a suitable reliability band for this physical parameter.

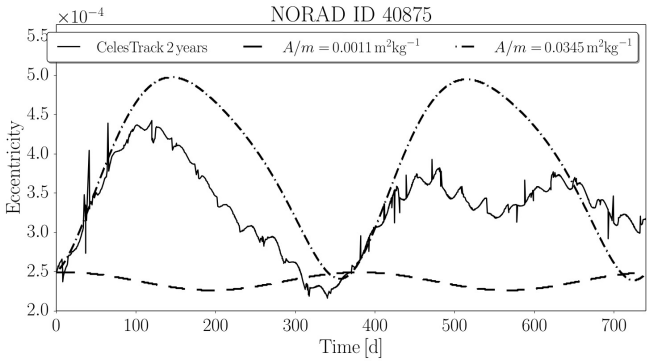

Figure 15: Temporal evolution of the eccentricity during 2 years of the orbiter with NORAD ID 40875. The CelesTrack data are represented with the solid line. A suitable reliability band for A/m ratio is 0.0011-0.0345 $\mathrm{m^2kg^{-1}}$, represented with the dashed lines, and computed with the analytical method.

5. Conclusion

The relative motion of different orbiters in the geostationary ring was illustrated by using the information of several observations taken from the Venezuelan National Observatory. Those relative orbits show that, space objects that are close each-other are affected by the same perturbing forces and move in a different way. A possible explanation could be its intrinsic physical nature, for example the area-to-mass ratio parameter. An analytical approach allows to understand how this parameter influences in the temporal evolution of an space object, even more if they are located at the geostationary region, where the solar radiation pressure can become one of the most important perturbations if the area-to-mass ratio of the object is big enough. In this work two different results are presented and both pursue the same objective, which is to obtain intrinsic physical characteristics of an space object by just knowing its ephemerides. Thus, given real ephemerides of space objects taken from CelesTrack database. The first result consists of associating an invented area-to-mass ratio to a space object and give a reliability band for this parameter by just analyzing the temporal evolution of the eccentricity. The second result consists of plotting the temporal evolution of the eccentricity of a space object by considering the CelesTrack data and derive a possible value for the area-to-mass ratio of the real space object. Thus, we illustrate an innovative way to obtain a physical property of a space object just by observational means.

6. Acknowledge

This work was partially supported by the Spanish Ministry of Economy and Competitiveness, Project no.ESP201787113−R (AEI/FEDER, UE) and by the Aragon Government and European Social Fund (group E24_17R).

References

Adushkin V., et al., 2016, Acta Astronautica, 126, p. 510
Alby F., et al., 2004, Adv. Space Res., 34, p. 1143
Africano J., et al., 2000, Space Debris, 2, p. 357
Agapov V., Molotov I., Khutorovsky Z., 2009, 10th Adv. Maui Opt. Space Surveillance Technol. Conf. on Space Debris, Hawaii
Anselmo L., Pardini C., 2002, Space Debris, 2, p. 67
Capderou M., 2005, Satellites Orbits and Missions, Springer-Verlag, France, p. 554
Casanova D., Petit A., Lemaître A., 2015, Celest. Mech. Dyn. Astr., 123, p. 223
Celletti A., et al., 2017, Inter. J. Non-Linear Mechs, 90, p. 147
Chovotov V., Herman D., Johnson C., J. Space. Rocket. 34 p. 233
Colombo C., Gkolias I., 2017, Proc. 7th ESA Space Debris Office, p. 1
Englert C., et al., 2014, Acta Astronautica, 104, p. 99
European Space Agency., 2019, ESAs Space Debris Office, Tech. Rep., 19, p. 179
Flohrer T., et al., 2005, Adv. Space Res., 35, p. 1226
Früh C., Schildknecht T., 2012, MNRAS, 419, 4, p. 3521
Hanada T, Yasaka T., 2002, J. Spacecraft and Rockets, 39, 1, p. 92
Inter Agency Space Debris Coordination Committee, 2007, IADC-02-01, 22, p. 10
Johnson N., et al., 2001, Adv. Space Res., 28, 9, p. 1377
Johnson N., et al., 2008, JSC 62530, NASA/TM, 214779, p. 504
Johnson N., 2012, Acta Astronautica, 80, p. 82
Klinkrad H., 2006, Space Debris Models and Risk Analysis, Springer, Berlin, Germany, p. 416
Krisko P., et al., 2015, Acta Astronautica, 113, p. 204
Kuznetsov E., Zakharova P,. 2015, Adv. Space Res., 56, p. 406
Laas-Bourez M., et al., 2011, Adv. Space Res., 47, p. 402
Lacruz E., Abad C., 2015, Rev. Mex. Astron. Astrofis, 46, p. 87
Lacruz E., et al., 2018, Rev. Mex. Astron. Astrofis, 50, p. 62
Lacruz E., et al., 2018, Rev. Mex. Astron. Astrofis, 50, p. 34
Lacruz E., et al., 2018, Rev. Mex. Astron. Astrofis, 54, p. 209
Lewis H., et al., 2001, Proc. 3th ESA Space Debris Office-473, 1, p. 373
Nuñez J., et al., 2015, Adv. Space Res., 56, p. 218
McKnight D., Di Pentino F., 2013, Acta Astronautica, 85, p. 73
Montenbruck O., Gill, E., 2005, Springer, p. 369
Morando B., 1963, Bull. Astron., 24, p. 47
Pardini C., Anselmo L., 2008, Trans. Japan. Soc. Aero. Space Sci., 51, 171, p. 22
Petit A., et al., 2018, Celest. Mech. Dyn. Astron., 130, 12, p. 79
Pradhan B., Hickson P., Surdej J., 2019, Acta Astronautica, 164, p. 77
Rykhlova L., et al., 2001, Adv. Space Res., 28, 9, p. 1301
Schildknecht T., et al., 2004, Adv. Space Res., 34, p. 901
Schildknecht T., 2007, Astron. Astrophys Rev., 14, p. 41
Schildknecht T., Musci R., Flohrer T., 2008, Adv. Space Res., 41, p. 1039
Smirnov N., 2002, Space Debris Hazard Evaluation and Mitigation, Taylor and Francis Publ., New York-London, p. 229
Soop E., 1994, Handbook Geostationary Orbits, Space Technology Library, Springer Netherlands, p. 309
Tapley D., et al., 1996, J. Geophys. Res., 101, p. 28029
Thomasson D., Deleflie F., Petit A., 2019, Acta Astronautica, 161, p. 115
Valk S., Lemaître A., Anselmo L., 2008, Adv. Space Res., 41, p. 1077
Valk S., et al., 2009, Adv. Space Res., 43, p. 1509
Wytrzyszczak I., Breiter S,. Borczyk W., 2007, Adv. Space Res., 40, p. 134